MCAT Institute
Final Report 92-003

INCOMPRESSIBLE VISCOUS FLOW COMPUTATIONS FOR THE PUMP COMPONENTS AND THE ARTIFICIAL HEART

Dr. Cetin Kiris

March 1992

NCC2-500

MCAT Institute
3933 Blue Gum Drive
San Jose, CA 95127

COMPUTATION OF INCOMPRESSIBLE VISCOUS FLOWS THROUGH TURBOPUMP COMPONENTS

Cetin Kiris

Abstract

A finite-difference, three dimensional incompressible Navier-Stokes formulation to calculate the flow through turbopump components is utilized. The solution method is based on the pseudocompressibility approach and uses an implicit-upwind differencing scheme together with the Gauss-Seidel line relaxation method. Both steady and unsteady flow calculations can be perfomed using the current algorithm. In this work, the equations are solved in steadily rotating reference frames by using the steady-state formulation in order to simulate the flow through a turbopump inducer. Eddy viscosity is computed by using an algebraic mixing-length turbulence model. Numerical results are compared with experimental measurements and a good agreement is found between the two. Time-accurate calculations, such as impeller and diffusor interaction, will be reported in future work.

Introduction

With the advent of supercomputer hardware as well as fast numerical methods, computational fluid dynamics (CFD) has become an essential part of aerospace research and design. Numerical studies in incompressible flows show good progress in parallel with computational studies in compressible flows. For example, the incompressible flow solver developed by Kwak et al [1] was extensively used for simulating the flow through space shuttle main engine power head components. The redesign of the space shuttle main engine hot gas manifold, guided by the computations of Chang et al. [2], illustrates the usefulness of CFD in aerospace research. Since the incompressible Navier-Stokes formulation does not yield the pressure field explicitly from the equation of state or through the continuity equation, numerical solution of the equations requires special attention in order to satisfy the divergence-free constraint on the velocity field. The most widely used methods which use primitive variables are fractional-step and pseudocompressibility techniques. In the fractional-step method, the auxiliary velocity field is solved by using the momentum equations. Then, a Poisson equation for pressure is formed by taking the divergence of the momentum equations and by using a divergence-free velocity field constraint. Solving the Poisson equation for pressure efficiently in three-dimensional curvilinear coordinates is the most important feature of the fractional step method.[3] One way to avoid the numerical difficulty originated by the elliptic nature of the problem is to use a pseudocompressibility method. With the pseudocompressibility method, the elliptic-parabolic type equations are transformed

into hyperbolic-parabolic type equations. Well established solution algorithms developed for compressible flows can be utilized to solve the resulting equations.

Steger and Kutler[4] employed an alternating direction implicit scheme into Chorin's[5] pseudocompressibility method. This formulation was extended to three-dimensional generalized coordinates by Kwak.[1] Recently, a three-dimensional incompressible Navier-Stokes solver (INS3D-LU-SGS) using a lower-upper symmetric-Gauss-Seidel algorithm was developed by Yoon and Kwak.[6] This algorithm is used to calculate the inducer flow of the Space Shuttle Main Engine turbopump in order to demonstrate the performance of the numerical method.[7] Another effort is performed in Ref. 8 by using upwind differencing and Gauss-Seidel line relaxation scheme in order to have a robust and fast converging scheme (INS3D-UP). A time accurate formulation of this algorithm is implemented for incompressible flows through artificial heart devices with moving boundaries.[8,10] In the present study, the steady-state formulation is used in steadily rotating reference frames in order to develop a CFD procedure for simulating the flow through turbopump components of a liquid rocket engine.

Computed Results

The flowfield through a turbopump inducer is solved as a benchmark problem in order to validate the CFD procedure for turbomachinery applications. In this section results obtained for the Rocketdyne inducer shown in Fig. 1 are presented. The inducer geometry was developed and experimentally studied by the Rocketdyne Division of Rockwell International. The design flow is 2236 GPM with a design speed of 3600 RPM. In the computational study, tip-leakage effects are included with a tip clearance of 0.008 inches. The problem was nondimensionalized with a tip diameter of 6.0 inches and the average inflow velocity of 28.3 ft/sec. The Reynolds number for this calculation was 191,800. The upstream section of the inducer was taken as a two tip-diameter-long straight channel, as shown in Fig. 1. The bull-nose of the inducer was treated as a rotating wall and the cavity section was neglected. However, this region can be included by using an additional zone. An H-H grid topology with dimensions of 187 x 27 x 35 was used. A partial view of the surface grid is shown in Fig. 2. An H-type surface grid was generated for each surface using an elliptic grid generator. The interior region of the three-dimensional grid was filled using an algebraic solver coupled with an elliptic smoother. In the straight channel, the grid was generated for one-sixth of the cross-section of the tube. This grid was extended to the outflow section of the inducer between the blades. Periodic boundary conditions were used at the end points in the rotational direction. At inflow and outflow boundaries characteristic boundary conditions were employed. At the inflow, v and w velocity components were specified as zero and the total pressure was specified as constant. Axial velocity and static pressure were calculated from the characteristic relation and the total pressure relation. At the outflow, static pressure was specified and the velocity components were computed from the characteristics propagating from the interior region. The flow was taken at rest initially and the inducer was fully rotated impulsively. The solution was considered converged when the maximum residual dropped at least four orders of magnitude. This

was obtained in less than 500 iterations. Computer time required per grid point per iteration was about 1.4 x 10^{-4} sec.

Figure 3 illustrates the planes where the experimental measurements were taken by Rocketdyne. Axial and tangential velocity components and the flow angle were measured in planes A,B,C and D at various circular arcs from the hub to the tip region. At each plane, the comparison between experimental measurements and numerical results along three of the circular arcs is presented in this paper. A total velocity and a flow angle are compared against experimental data. The total velocity has only a tangential and an axial velocity components. The radial velocity component was not measured in the experiment.

Figures 4 through 7 show relative total velocities and relative flow angles as a function of circumferential angle in degrees in planes A, B, C, and D, respectively. The circumferential angle increases from the suction side to the pressure side. The dashed lines in these figures represent the experimental data and solid lines represent the numerical results. The comparison of computations and experiment is generally good all the way from the hub to tip region. The difference between experimental and numerical data is about 5-8 % in velocity. In all planes, the hub and tip regions indicate the biggest discrepancy. This may be a result of the relatively coarse grid used for the boundary layer. In the computational study, the Baldwin-Lomax algebraic turbulence model is used to determine the eddy viscosity. The comparison shows that the solution algorithm does a god job with an algebraic turbulence model. The implementation of the one equation model[11] of Baldwin and Barth is currently underway for the present algorithm. The motivation for higher-order turbulence modeling is due to the comparisons obtained in Plane D, in which the wake region is not predicted accurately (Fig. 7). Another advantage of the one-equation model is that there is no need to define a length-scale explicitly. Near the tip clearance region, the difference between experimental measurements and numerical results is noticably larger than the error in other regions. This is due to lack of grid resolution in the tip clearance region. In the grid refinement study, the number of grid points in the tip clearance region was increased from 4 points to 9 points. In the coarse grid computation, there is one overlapped grid point in the rotational direction to ensure periodic boundary conditions. In the fine grid, additional 3 zones were added in radial direction. The results with the one equation model and the results from the grid refinement study will be published in future.

Figure 8 shows the surface of the inducer colored by nondimensionalized pressure. The pressure gradient across the blades due to the action of centrifugal force and the pressure rise from inflow to outflow are illustrated. This pressure rise along the inducer can also be seen in Fig. 9. Velocity vectors are plotted in the meridional plane and the vectors are colored by the static pressure. The existing solution procedure can be applied to the same configuration under off-design conditions. The massive separation which may block the fuel supply can be detected in the numerical study. This is the future research area of the present study which can be used as a pre-design and post-design engineering tool in challenging turbomachinery applications.

Summary

An efficient and robust solution procedure is implemented and validated for three-dimensional turbopump applications. Numerical simulations of the flow through the Rocketdyne inducer have been successfully carried out by using CFD techniques for solving viscous incompressible Navier-Stokes equations with the source terms in steadily rotating reference frames. The method of artificial compressibility with a higher-order accurate upwind differencing and the Gauss-Seidel line relaxation scheme provide fast convergence and robustness. Results in the form of relative total velocity and relative flow angle in four planes are presented. Numerical results compare fairly well with experimental data.

References

[1] Kwak, D., Chang, J. L C., Shanks, S. P., and Chakravarthy, S., " A Three-Dimensional Incompressible Navier-Stokes Flow Solver Using Primitive Variables ", *AIAA Journal* , Vol 24, no. 3, pp. 390-396, 1977.

[2] Chang, J. L C.,Kwak, D., Rogers, S. E., and Yang, R.-J., " Numerical Simulation Methods of Incompressible Flows and an Application to the Space Shuttle Main Engine ", *Int. J. Num. Meth. in Fluids*, Vol 8, pp. 1241-1268, 1988.

[3] Rosenfeld, M. , Kwak, D. and Vinokur, M., " A Fractional Step Solution Method for the Unsteady Incompressible Navier-Stokes Equations in Generalized Coordinate Systems ", to Appear *Journal of Computational Physics* , 1991.

[4] Steger, J. L., Kutler, P., "Implicit Finite-Difference Procedures for the Computation of Vortex Wakes ", *AIAA Journal* , Vol 15, no. 4, pp. 581-590, Apr. 1977.

[5] Chorin, A., J., " A Numerical Method for Solving Incompressible Viscous Flow Problems ", *Journal of Computational Physics,* vol. 2, pp. 12-26, 1967

[6] Yoon, S., Kwak, D., " Three-Dimensional Incompressible Navier-Stokes Solver Using Lower-Upper Symmetric-Gauss-Seidel Algorithm", *AIAA Journal* , Vol 29, No 4, pp. 874-875, 1991

[7] Yoon, S., Kwak, D., " Implict Methods for the Navier-Stokes Equations", *Computing Systems in Engineering* , Vol 1, Nos 2-4, pp. 535-547, 1990

[8] Rogers, S. E., Kwak, D. and Kiris, C., " Numerical Solution of the Incompressible Navier-Stokes Equations for Steady and Time-Dependent Problems ", *AIAA Journal* , Vol 29, No 4, pp. 603-610, 1991

[9] Kiris, C., Chang, I., Rogers, S. E. and Kwak, D., " Numerical Simulation of the the Incompressible Internal Flow Through a Tilting Disk Valve", AIAA Paper 90-0682, 1990.

[10] Kiris, C., Rogers, S. E., Kwak, D. and Chang, I. " Computation of Incompressible Viscous Flows with Moving Boundaries", Proc. Intl. Symposium on Biofluiddynamics, July 6-12, 1991.

[11] Baldwin, B., S. and Barth, T., J., " A One-Equation Turbulence Transport Model for High Reynolds Number Wall-Bounded Flows ", AIAA Paper No. 91-0610, 1991.

Figure 1: Rocketdyne turbopump inducer configuration.

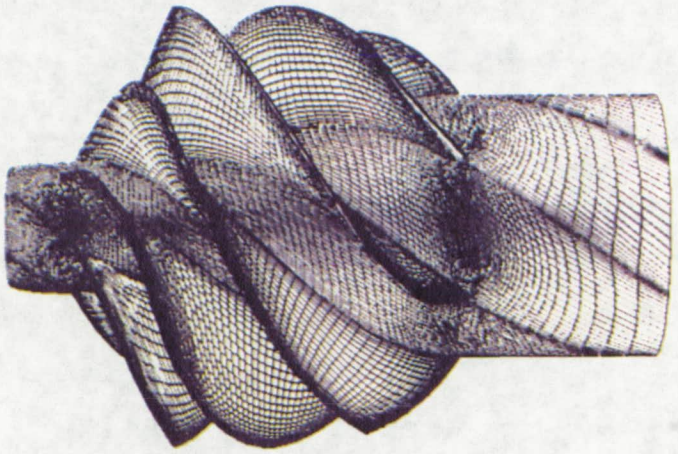

Figure 2: Surface grid for Rocketdyne turbopump inducer.

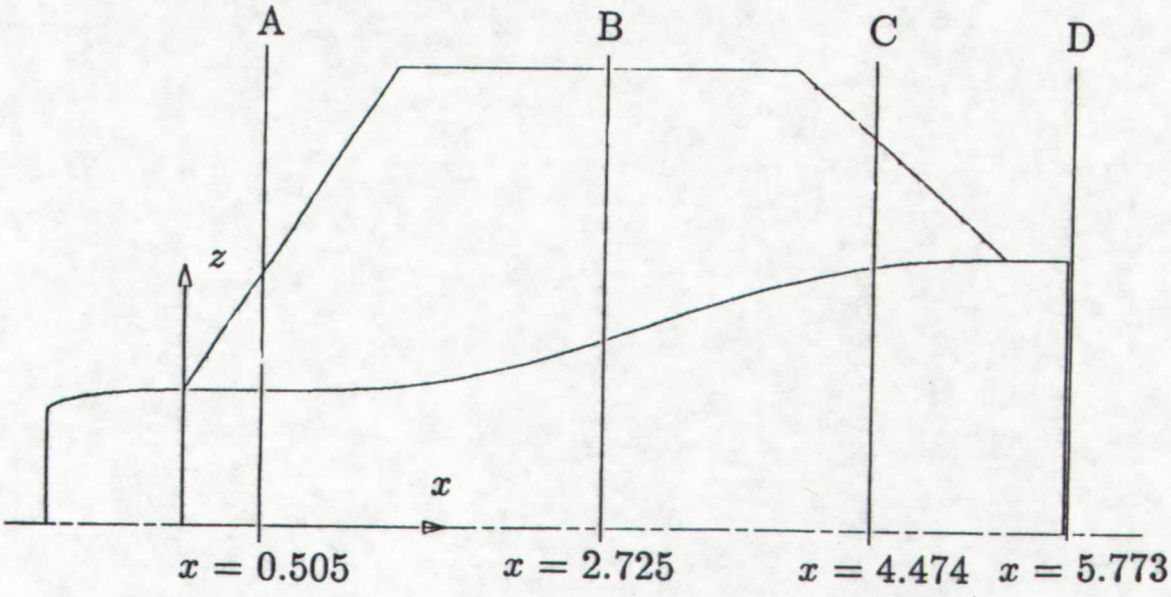

Figure 3: Schematic representation of the planes where experimental data is available.

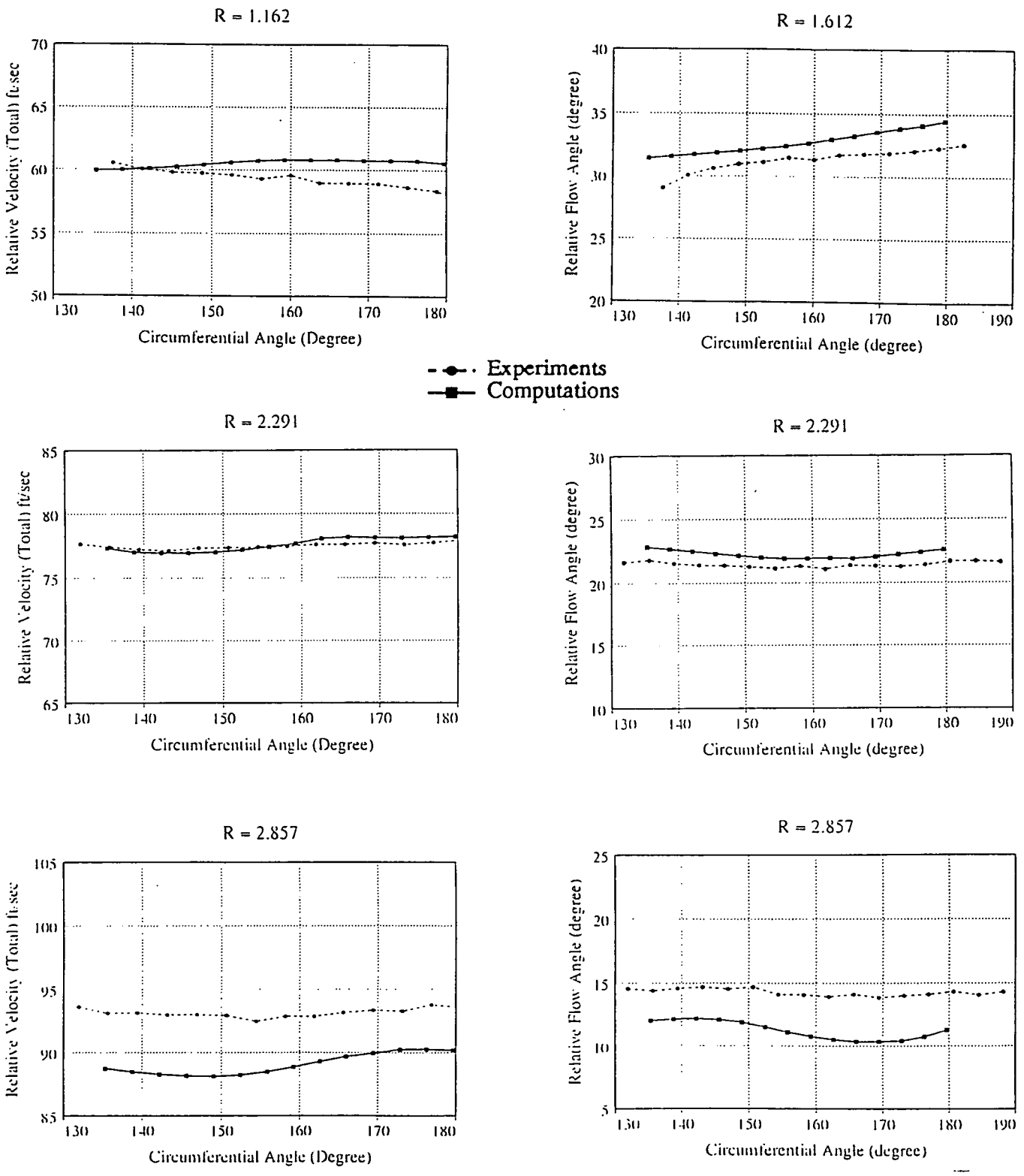

Figure 4: Comparison of relative total velocity and relative flow angle in Plane A.

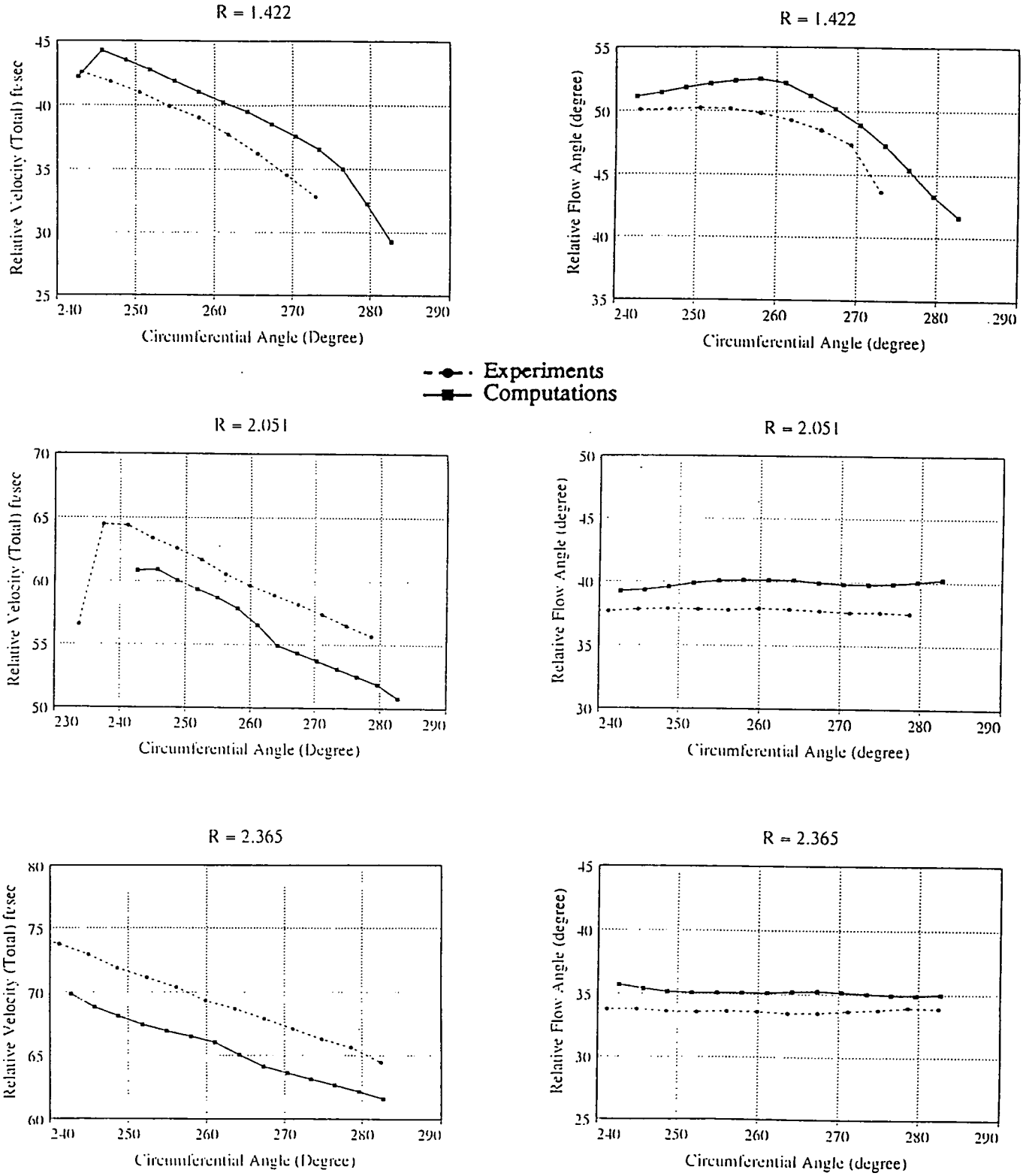

Figure 5: Comparison of relative total velocity and relative flow angle in Plane B.

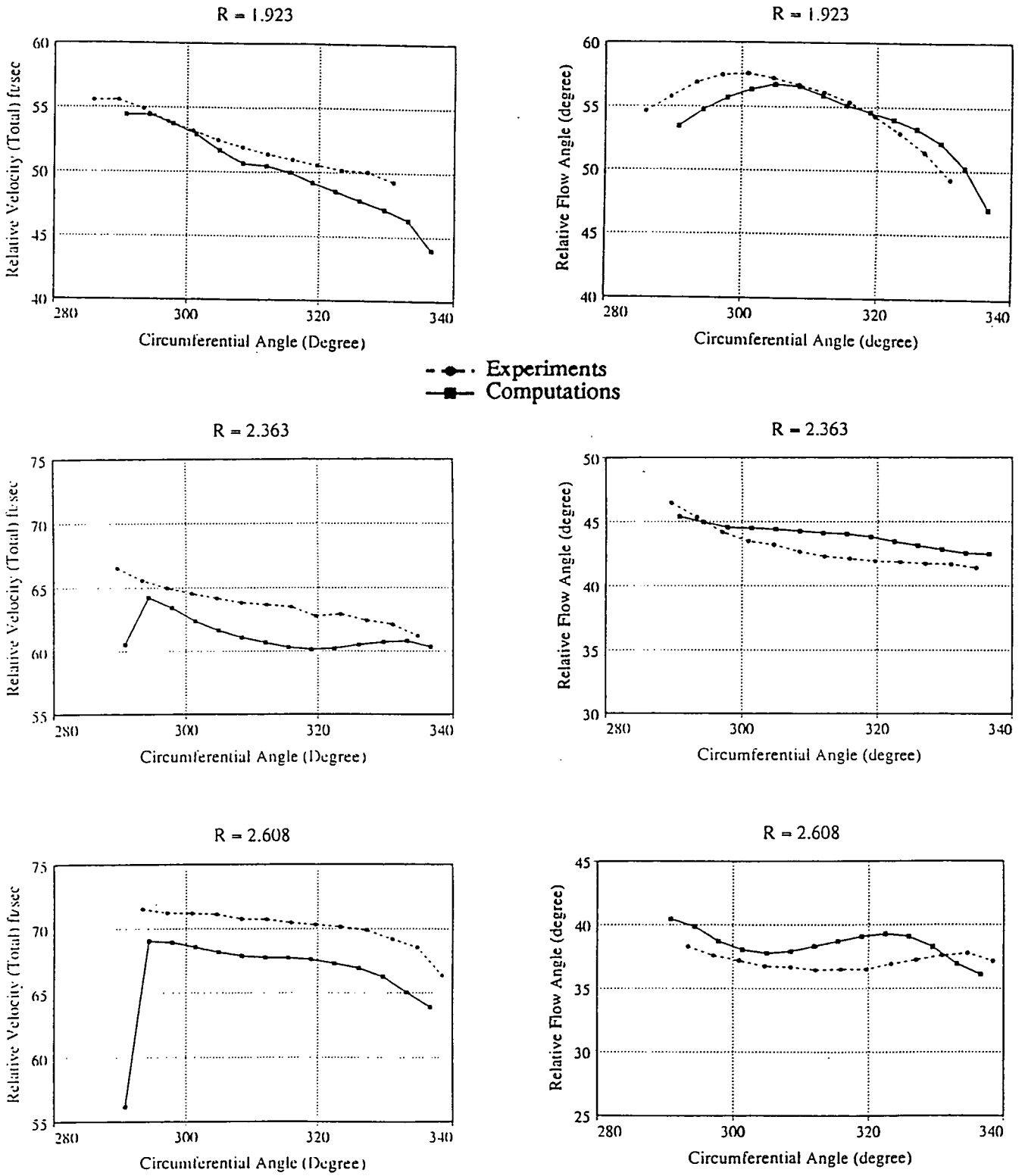

Figure 6: Comparison of relative total velocity and relative flow angle in Plane C.

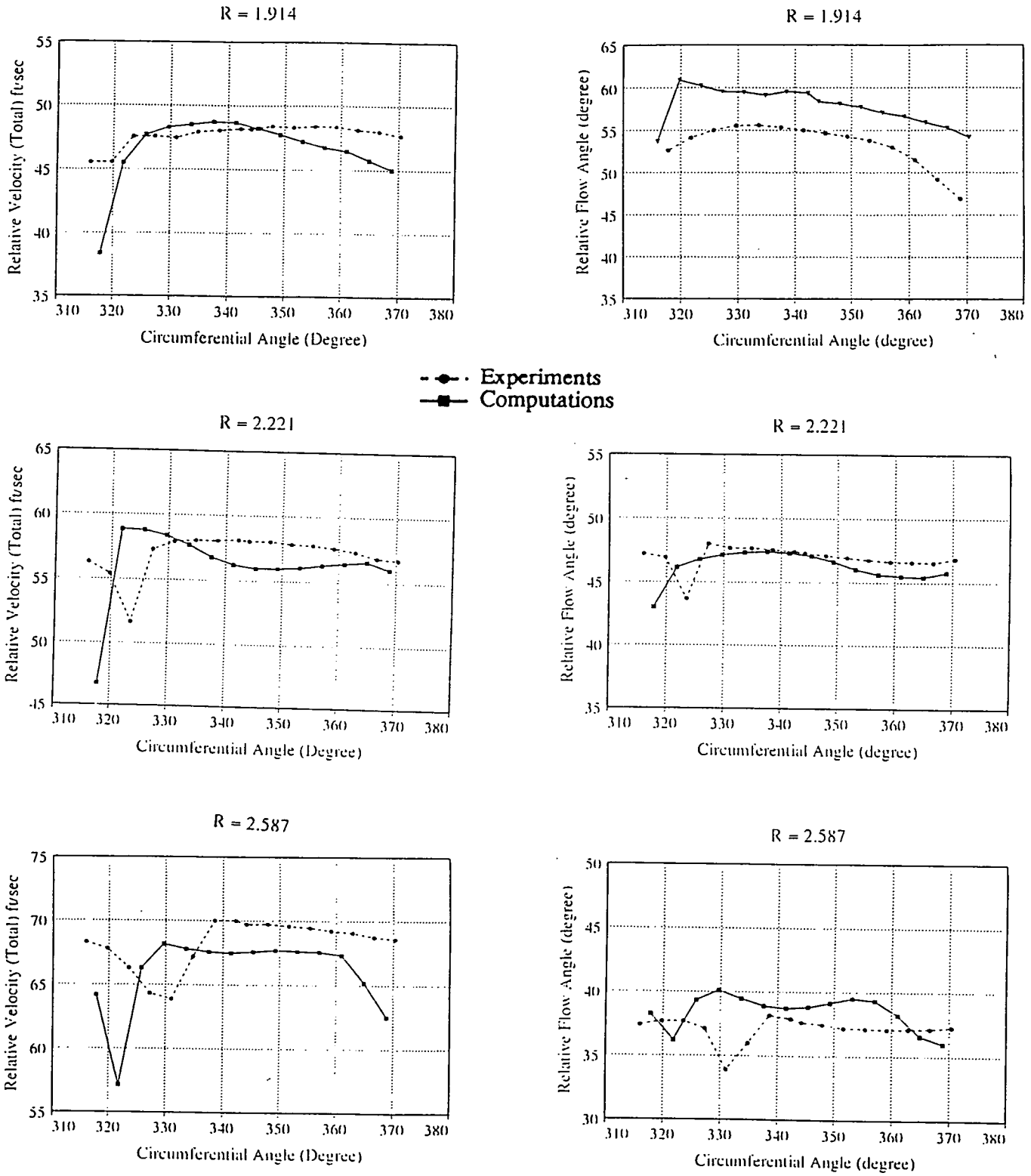

Figure 7: Comparison of relative total velocity and relative flow angle in Plane D.

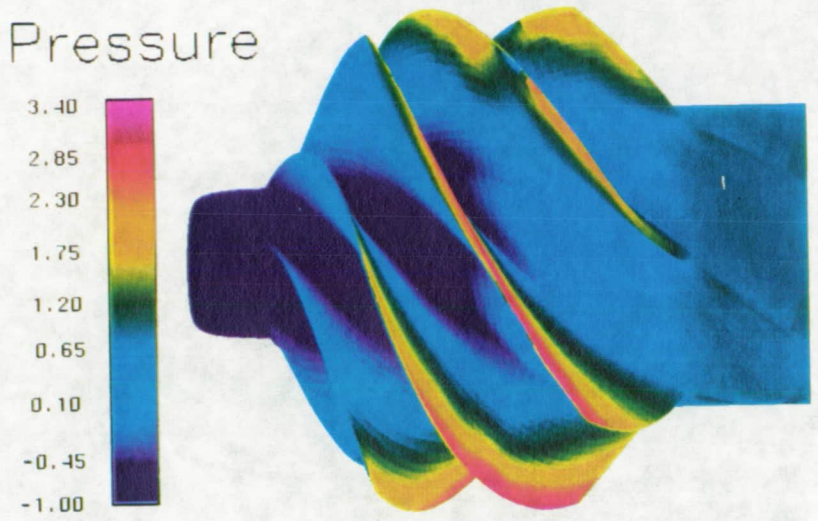

Figure 8: Surface pressure for Rocketdyne inducer.

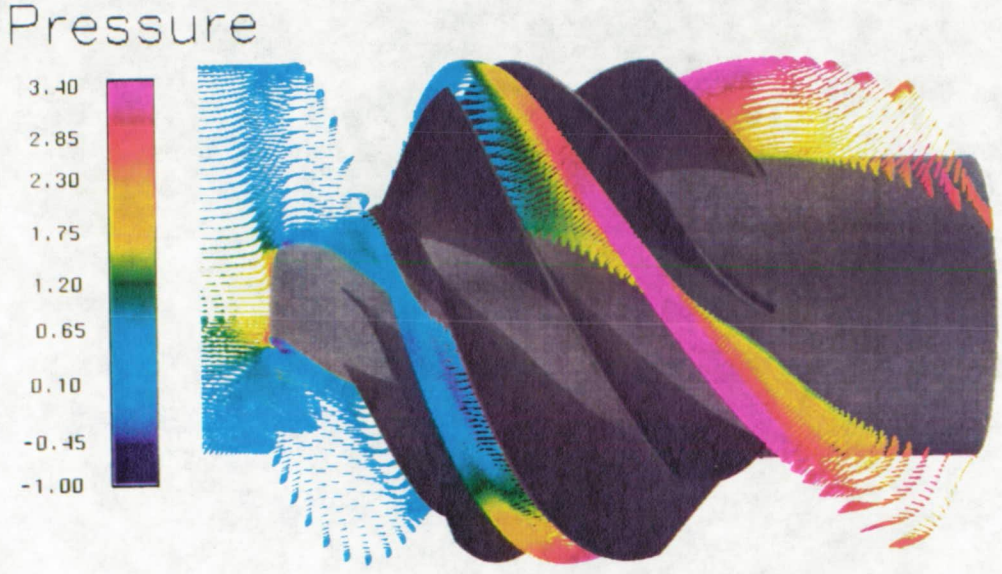

Figure 9: Velocity vectors colored by pressure on the meridional plane of the inducer.

APPENDIX

N16

Computation of Incompressible Viscous Flow Through Artificial Heart Devices with Moving Boundaries

C. Kiris, S. Rogers, D. Kwak
NASA Ames Research Center

and

I-Dee Chang
Stanford University

Proceedings American Mathematical Society Summer Research
Biofluiddynamics Conference
July 6-12, 1991, Seattle, WA

(To appear in ASME J. of Biofluidmechanical Engineering)

Contemporary Mathematics
Volume 00, 0000

Computation of Incompressible Viscous Flows Through Artificial Heart Devices with Moving Boundaries

CETIN KIRIS[†], STUART ROGERS[†],
DOCHAN KWAK[†], AND I-DEE CHANG[‡]

ABSTRACT. The extension of computational fluid dynamics techniques to artificial heart flow simulation is illustrated. Unsteady Navier–Stokes equations written in three-dimensional generalized curvilinear coordinates are solved iteratively at each physical time-step until the incompressibility condition is satisfied. The solotion method is based upon the pseudocompressibility approach and uses an implicit upwind differencing scheme together with the Gauss-Seidel line-relaxation method. The efficiency and robustness of the time-accurate formulation of the numerical algorithm are tested by computing the flow through model geometries. A channel flow with a moving indentation is computed and validated with experimental measurements and other numerical solutions. In order to handle the geometric complexity and the moving boundary problems, a zonal method and an overlapped grid-embedding scheme are employed, respectively. Steady-state solutions for the flow throufh a tilting-disk heart valve are compared with experimental measurements; good agreement is obtained. The flow computation during opening and closing of the valve is carried out to illustrate the moving-boundary capability. Aided by experimental evidence, the flow through an entire Penn State artificial heart model is computed.

1. Introduction

With the advent of supercomputer hardware, as well as fast numerical methods, researchers in the field of computational fluid dynamics (CFD) tackle more complicated problems than ever before. With these new capabilities, CFD has become an essential part of aerospace research and design. For example, the incompressible flow solver developed by Kwak et al. (Ref. 1) was extensively used

1991 *Mathematics Subject Classification.* Primary.
Supported in part by the NASA Technology Utilization Office.

0000-0000/00 $1.00 + $.25 per page

State electric artificial heart, can be well defined (Ref. 9). Therefore, the present study is focused on the fluid problem with prescribed body motion.

Underwood and Mueller obtained the flow characteristics for the Kay–Shiley disk-type valve by using the stream function-vorticity formulation (Ref. 10). Their results showed agreement with experimental data up to a Reynolds number of 600. Idelsohn et al. modeled the flow through the Kay–Shiley caged disk, Starr–Edwards caged ball, and Bjork–Shiley tilting-disk valves and compared their performance (Ref. 11). Turbulent flow through trileaflet aortic heart valves was simulated by Stevensen et al. (Ref. 12). Most numerical studies assumed that the flow through the heart valve was two-dimensional. Additionally, the valve opening and closing motions were neglected; only the flow through a fixed valve position was studied. In reality, the geometry is three-dimensional, and the flow through heart valves involves moving boundaries.

In our present study we propose the development of a computational procedure simulating steady and unsteady three-dimensional flows through artificial hearts and heart valves with moving boundaries. In the next sections, the method of solution is summarized followed by a demonstration of how this CFD procedure can be used for probing the flow through artificial heart devices.

2. Method of solution

The flow through artificial heart devices is unsteady, viscous, and incompressible. In the present study, the non-Newtonian nature of the blood is neglected, and the flow is described by the three-dimensional incompressible Navier–Stokes equations. Numerical simulation of such flows is a very challenging problem in computational fluid dynamics. In addition to the geometric complexity, obtaining time-dependent solutions of the incompressible Navier–Stokes equations with moving boundaries poses many difficult numerical problems.

Because the pressure and velocity fields are not directly coupled owing to the lack of a pressure term in the continuity equation, numerical solution of the incompressible Navier–Stokes equations requires special attention in order to satisfy the divergence-free constraint on the velocity field. The most widely used methods that use primitive variables are fractional-step and pseudocompressibility techniques. In the fractional-step method, the auxiliary velocity field is solved by using the momentum equations. Then, a Poisson equation for pressure is formed by taking the divergence of the momentum equations and by using a divergence-free velocity field constraint. The efficient solution of the Poisson equation for pressure in three-dimensional curvilinear coordinates is the most important feature of the fractional-step method (Ref. 13). One way to avoid the numerical difficulty originated by the elliptic nature of the problem is to use a pseudocompressibility method. With the pseudocompressibility method, the elliptic-parabolic-type equations are transformed into hyperbolic-parabolic-type equations. Well-established solution algorithms developed for compressible flows can then be utilized to solve the resulting equations.

In the present study, the pseudocompressibility approach is used and the time-accuracy is attained by iterating in pseudo-time until the divergence of velocity is driven toward zero to within a specified tolerance. Here, the time-derivatives in the momentum equations are differenced by using a second-order, three-point, backward-difference formula. The numerical method uses a second-order central-difference for viscous terms and a higher-order flux-difference splitting for the convective terms. The resulting matrix equation is solved iteratively by using a nonfactored line-relaxation scheme, which maintains stability and allows a large pseudo-time-step to be taken. At each sweep direction, a tridiagonal matrix is formed, and off-line terms of the matrix equation are moved to the right-hand side of the equation. Details of the governing equations and numerical method are given in References 14 and 15.

One of the biggest difficulties in the simulation of flows in complicated three-dimensional configurations is the discretization of the physical domain. The problem becomes more severe if one body in the domain of interest moves relative to another one, as is seen in the tilting disk valve and the Penn State artificial heart geometries. The use of a zonal approach is a practical solution if the grids are stationary. For more general applications, a chimera grid-embedding technique provides a greater flexibility for the grid motion (Ref. 16). This technique is employed for flow computations through a tilting disk valve and the Penn State artificial heart model.

3. Computed results

One of the goals of this study is to simulate the flow through a realistic model of an artificial heart. Since the geometry and the flow physics are complicated, the computational procedure is validated by solving several simpler problems which characterize the flow in various parts of an artificial heart. As a first step, an idealized two-dimensional pump model was chosen to demonstrate the capability of the time-accurate formulation under a moving grid-condition. The geometry of this model and the computed results are presented in Reference 14. Channel flow with an identical wall, the flow through a tilting-disk heart valve, and the flow through the Penn State artificial heart model are included in this section.

3.1 Channel flow with a moving indentation.

Channel flow with an asymmetric oscillating indentation was experimentally studied by Pedley and Stephanoff and was numerically simulated by Ralph and Pedley (Ref. 18). In the experiment, the channel was was rigid everywhere except for the indentation, which is made of a thick rubber membrane. The experiment shows that flow is two-dimensional near the midplane, and so the computation is done in two dimensions.

Figure 1 illustrates the instantaneous streamlines plotted at several nondimensional times for Reynolds number $Re = 600$ and for Strouhal number $St = 0.057$.

The Reynolds number is based on the channel height a, and on the average velocity at the entrance of the channel $\overline{U}$. The Strouhal number is defined as $St = af/\overline{U}$, where f is the oscillation frequency. At the beginning of the cycle, the flow downstream of the indentation is parallel to the channel walls. A single eddy is formed at the sloping wall of the indentation during the first half of the cycle. The streamlines at the core flow are lifted slightly upward as shown in Figure 1a. This is the beginning of the wavy flow patterns of the core flow. The formation of a second separated eddy on the opposite wall can be seen in Figure 1b. In later stages, the double row of eddies along the lower and upper wall of the channel is observed. At the end of the cycle, the vortices are swept downstream (Fig. 1g), and the residual vortices are not strong enough to affect the next cycle. In fact, the flow pattern of the first and second cycles are quite similar. Consequently, the flow is assumed to be periodic in time, even at the first cycle. Another interesting phenomenon observed in the present study, as well as in the experimental and other numerical studies, is the eddy-doubling which can be seen in Figures 1c through 1e. It occurred in the second, third, and fourth vortices from the indentation. In eddy-doubling, a single eddy splits into two rotating eddies.

The time-evolution of the centers of the vortices is compared with experimental and other numerical findings. The first four vortices are labeled vortices A, B, C, and D, and are shown in Figure 2b. The distance between the indentation wall and the center of these vortices is measured from the instantaneous streamlines and plotted versus time in Figure 2a. The dashed lines represent the present computations. The solid lines denote computational results from the fractional-step approach implemented by Rosenfeld (Ref. 19). Dotted lines are numerical results of stream-function vorticity formulations from Ralph and Redley (Ref. 18). Experimental measurements by Pedley and Stephanoff (Ref. 17) are represented by square symbols. The agreement between the numerical and experimental measurements is fairly good. There is a discrepancy between the numerical results and experimental measurements about the location of the vortex A. The present results and Rosenfeld's computations predict the location of vortex A to be 0.4 units closer to the indentation than the experimental findings. However, the locations of the remaining vortices are correctly predicted, if the distance is measured from the center of the vortex A. This underprediction of the separation length of vortex A is thought to be caused by an inaccurate description of the indentation wall shape. In the present study and in Rosenfeld's study the same grid and the same wall shape were used. Even though the solution algorithms of the two computational studies are completely different, the agreement between the numerical results is good. For these reasons, only the locations of vortices B, C, and D are compared with the experimental measurements.

3.2 Flow through tilting disk valve.

The problem of flow through the tilting-disk valve was chosen to develop and

validate a procedure that will be used for the valve region of the Penn State artificial heart. In the Bjork–Shiley tilting-disk heart valve, the tilting disk is placed in front of the sinus region of the human aorta. The aortic root has three sinuses about 120° apart. The tilting-disk valve model used in this computation is simplified by assuming that the sinus region of the aorta has a circular cross section. The cage and struts which hold the free-floating disk inside of the sewing ring are not included in the geometry. It is also assumed that the walls have no elastic deformation. The channel length is taken to be five aorta diameters long. The computational geometry used in these unsteady flow computations is given in Figure 3. The disk motion is illustrated by showing three different positions of the disk, at angles of 75°, 50°, and 30°, as measured from the centerline of the aorta. The tilting disk is allowed to rotate about the horizontal axis, which is 1/6 of a disk diameter below the center of the disk. Because of this asymmetric disk orientation, the flow is three dimensional.

The chimera grid-embedding technique, which has been successfully used for external flow problems, has been employed by using two overlapped grids, as shown in Figure 4. Grid 1 occupies the whole region in the aorta from entrance to exit, and remains stationary. Grid 2 wraps around the tilting disk, and moves with the disk. In the chimera grid-embedding technique, grid points that lie within the disk geometry and outside the channel grid are excluded from the solution process. These excluded points are called hole points, and the immediate neighbors of the hole points are called fringe points. The information is passed from one grid to another via fringe and grid boundary points by interpolating the dependent variables. Tri-linear interpolation is used in the present computations. In order to distinguish the hole and fringe points from regular computational points, an IBLANK array is used in the flow solver. For hole, grid boundary, and fringe points, IBLANK is set to zero; otherwise it is set to one. In order to exclude the hole and grid boundary points from the solution procedure, the coefficients of the system of algebraic equations and the right-hand-side terms are multiplied by the IBLANK value. If the grid point is a hole, an outer boundary, or a fringe point, the value of (1 - IBLANK) is added to the main diagonal of the matrix equation.

Presented here are the results of steady flow with a fixed disk angle and unsteady flow with the disk motion in the configuration described above. The problems are nondimensionalized by using the entrance diameter as a unit length, and the average inflow velocity as the unit velocity. In order to reduce the computational effort and memory size, the inflow and outflow boundaries are placed a short distance from the region of interest relative to the boundaries used in the experimental studies. In addition, the exact shape of the sinus region of the aorta used in the experiments is not known. These discrepancies could lead to slight differences between the present computations and experimental results.

Steady-state calculations for the 30° disk orientation have been carried out for Reynolds numbers in the range of 2,000 to 6,000, for which experimental data

are available. The Reynolds number is based on the diameter and the mean velocity at the entrance of the channel. A mixing-length algebraic turbulence model, which is used for incompressible flow through the space shuttle main-engine turnaround duct (Ref. 2), is utilized. Figure 5 shows the pressure drop across the Bjork–Shiley tilting-disk valve at different flow rates of physiological interest. The computed and measured axial velocity profiles at 42 mm downstream from the disk are shown in Figure 6. Axial velocity profiles are plotted in the horizontal plane through the center of the channel. The numerical results are shown with dots, and the experimental results are shown with triangles. The numerical results compare favorably with the experimental measurements (Ref. 3). The largest discrepancy is seen near the walls, where the boundary layer is overestimated by the calculation. Figure 7 shows the velocity vectors at five longitudinal stations. The flow, which is directed to the upper part of the aorta, generates vortices in the sinus region of the aorta and a large separated region along the lower wall of the aorta. Since separated-flow and low-flow regions have the potential to form thrombi, clotting may occur on the upper sinus region and the lower wall of the aorta. Figliola and Mueller also present mean velocity profiles, which show similar flow characteristics to those indicated by computational study, at several locations (Ref. 5). They computed the shear stress from the measured velocity field and observed that the maximum shear occurs at the top wall downstream of the sinus region of the aorta. This is in agreement with the velocity plot shown in Figure 7, in which there are large velocity components just off the wall in that location. Particle traces in Figure 8 indicate that the flow does not separate adjacent to the tilting disk. The tilting disk separates the flow into a major flow region, which is along the upper wall of the tube, and a minor flow region, which is along the lower wall of the tube. Separation, reverse flow, and swirling motion mostly occur in the minor flow region.

Figure 9 shows vorticity magnitude contours in the surface of the tube, outflow surface, and inflow surface of the disk, respectively. It is assumed that maximum vorticity magnitudes indicate the regions of high shear. The sewing ring surface and the edges of the disk are the regions where the vorticity magnitude is at a maximum. The upper wall of the channel also has high vorticity magnitudes.

Unsteady-flow calculations have been carried out in order to demonstrate and analyze the flow during opening and closing of the disks. For the present computations, one cycle of valve opening and closing requires 70 physical time-steps. During each time-step, subiterations are carried out until both the maximum divergence of velocity and the maximum residual drop below 10^{-3}. The computing time required for one cycle of the valve opening and closing is approximately 5 Cray-YMP hours. During the valve opening, inflow velocity is imposed at the entrance of the channel The inflow velocity is chosen as a sine function in time. The disk rotation is specified as a linear function in time. Since the forces acting on the disk are known from the numerical solution, the disk rotation angle can be determined. However, the disk rotation angle is limited. For large disk-rotation

angle, some information may be lost between the grids when the grid-embedding technique is used. In order to prevent the information loss, the maximum allowed disk-rotation angle at each physical time-step is taken to be less than 3°.

Figures 10a through 10c illustrate the velocity vectors on the lateral symmetry plane at $t/T = 0.128$, 0.257, and 0.385, respectively. The velocities are very high in the region between the disk and the channel wall, as shown in Figure 10a. During the disk opening, two vortices are formed at the upper and lower edges of the disk. The flow starts to separate behind the disk and reattaches to the wall as shown in Figure 10b. The stagnation region behind the disk moves downstream as the disk rotates. Highly skewed velocity profiles are seen downstream from the disk, as illustrated in Figure 10c. The growth of the vortices has also been observed in the sinus region of the aorta while the flow opens the valve. Along the lower wall a separation region is formed.

3.3 Artificial heart flow.

The Penn State artificial heart model is composed of a cylindrical chamber with two tube extensions (Fig. 11). The inflow (mitral) and outflow (aortic) tubes contain concave tilting disks, which open and close to act as valves. In the computational model, tilting-disk mitral valve orientation in time was obtained from the experimental data provided by Pennsylvania State University. The aortic valve orientation in time was approximated to mitral valve orientation with a phase difference. The pumping action is provided by a pusher plate whose velocity is sinusoidal in time. The diameter of the pusher plate is 7.26 cm, and it has a stroke length of 2.28 cm. The problem is nondimensionalized with the inflow tube diameter, which is 2.54 cm, and a unit velocity of 20 cm/sec. In the computational study, the Reynolds number based on the unit length and velocity is 900. Initially, the flow was started at rest, and four cycles of the pumping action were completed using a Cray-YMP computer at NASA–Ames Research Center. One cycle of the pusher plate's motion required 240 physical time-steps. At each time-step, the equations were iterated until the maximum divergence of velocity was reduced below 10^{-2}. During most of the cycle, 10–20 subiterations were required (for more detail, see Refs. 14, 15).

In order to handle the geometric complexity and the moving boundary-problems, a zonal method and an overlapped grid-embedding scheme (Ref. 16) are employed, respectively. In the zonal method, a complex computational domain is divided into several simple subdomains. The overlapped grid-embedding scheme allows subdomains to move relative to each other, and provides great flexibility when the boundary movement creates large displacements. The computational grid for the heart model is shown in Figure 11. Grid 1 is generated for the pusher plate and moves with it. Grid 2 occupies the chamber and remains stationary. Grids 3 and 5 are for the inflow and outflow tube extensions, respectively. Grid points for the tubes and grid points for the chamber are overlapped on three common planes. In other words, the grid points for the tubes start three stencils inside of the chamber outer boundaries. Zonal boundary conditions are used in

the interface boundaries. Grids 4 and 6 wrap around tilting disks, and move with the disks. An overlapped grid-embedding scheme is employed between moving grids and stationary grids.

The purpose of the computed results presented next is mainly to demonstrate how CFD can be used to understand the flow in the artificial heart, and the comparison with experiment is qualitative. Unsteady particle traces are illustrated in Figure 12. The particles are released near the inflow valve at the beginning of the fourth cycle. The figure is plotted at nondimensional time $t/T = 0.45$ into the period at which time the pusher plate is close to its lowest position, where T denotes the period for the pusher plate's motion. Figure 12 shows that the flow creates a strong vortex in the center region of the chamber. The particles have a swirling motion against the back wall against the mitral valve opening. The flow also separates at the connection region of the chamber and the inflow tube. Figure 13 shows the computed velocity vectors on the horizontal midplane at nondimensional time 0.375. At that time, the pusher plate is moving down, and the mitral valve is open. Figure 13 also indicates the presence of strong circulation in the chamber. However, the three-dimensional structure of the flow cannot be seen clearly, because the vectors are plotted on a two-dimensional plane.

The strong vortex in the center of the chamber is actually created where the chamber and the inflow tube are connected. The vortex moves to the core of the chamber in time. Experimental measurements by Baldwin and Tarbel (Ref. 19) are illustrated in Figure 14. Since the computational study does not include the blood sac inside the chamber, the comparison of experimental and computational results is qualitative. In addition, the Reynolds number in the experimental study is 1.7 times larger than the Reynolds number in the computational study, because the flow is assumed to be laminar in the present computations. The biggest discrepancy between experimental measurements and computational results is the location of the vortex core in the chamber. In Figure 13, the vortex is off-center in the chamber. In Figure 14, the vortex is located almost in the center of the chamber. Another difference can be seen in the wake region of the mitral valve. Since the Reynolds number in the computational study is lower, the wake is not as strong as the wake in Figure 14. The Reynolds number in the future computational study will be increased by including the turbulence modeling in order to have a quantitative comparison between experimental and computational results.

During the second half of the cycle time, the pusher plate moves upward, and the outflow valve is opened. A top view of the computed velocity vectors on the horizontal plane at $t/T = 0.625$ is plotted in Figure 15. Since the inflow valve is closed, residual eddies are quite large near the disk. However, they are quickly weakened as the pressure builds up inside the chamber. Measured velocity vectors at $t/T = 0.625$ are shown in Figure 16.

Figure 17 shows additional vortex structures in the vertical plane of the cham-

ber at nondimensional time 0.25. That vortex structure causes the swirling motion of the particles previously shown in Figure 12. The swirling flow in the outflow tube is shown in Figure 18. The velocity vectors in the cross-sectional plane of the outflow tube at $t/T = 0.75$ are plotted. The cross-sectional plane is one nondimensional unit downstream of the tilting-disk valve, and the normal vector of that cross section is in the positive x-direction shown in Figure 13.

4. Summary

An efficient and robust solution procedure is developed and validated for numerical simulations for internal flows through artificial heart devices. The solution procedure for unsteady, incompressible, viscous flow computations has been extended with the incorporation of the grid-embedding approach. This has been used to simulate the flow through a tilting-disk heart valve and the flow through the Penn State artificial heart model. Separated and secondary flow regions have been pointed out in the tilting-disk heart valve and artificial heart flow simulations. The vortex created in the central portion of the Penn State artificial heart provides good wall washing over the entire chamber. The present capability of simulating complicated internal flow problems with moving boundaries is demonstrated. The procedure developed in this study is quite general and is applicable to various types of artificial heart and valve geometries. It is hoped that artificial heart researchers and designers may further benefit from the computational ability obtained in the current work.

References

1. Kwak, D.; Chang, J. L C.; Shanks, S. P.; and Chakravarthy, S.: A Three-Dimensional Incompressible Navier–Stokes Flow Solver Using Primitive Variables. AAIA Journal, vol. 24, no. 3, 1977, pp. 390–396.
2. Chang, J. L C; Kwak, D.; Rogers, S. E.; and Yang, R.–J.; Numerical Simulation Methods of Incompressible Flows and an Application to the Space Shuttle Main Engine. Int. J. Num. Meth. Fluids, vol. 8, 1988, pp. 1241–1268.
3. Yoganathan, A. P.; Concoran, W. H.; and Harrison, E. C.: In Vitro Velocity Measurements in the Vicinity of Aortic Prostheses. J. Biomechanics, vol. 12, 1979, pp. 135–152.
4. Yoganathan, A. P.; Concoran, W. H.; and Harrison, E. C.: Pressure Drops Across Prosthetic Aortic Heart Valves under Steady and Pulsatile Flow. J. Biomechanics, vol. 12, 1979, pp. 153–164.
5. Figliolla, R. S.; and Mueller, T. J.: On the Hemolytic and Thrombogenic Potential Occluder Prosthetic Heart Valves from In Vitro Measurements. J. Biomech. Engng., vol. 103, 1981, pp. 83–90.
6. Peskin, S. C.; and McQueen, D. M.: Modeling Prosthetic Heart Valves for Numerical Analysis of Blood Flow in the Heart. J. Comput. Phys., vol. 37, 1980, pp. 113–132.
7. McCracken, M. F.; and Peskin, S. C.: A Vortex Method for Blood Flow through Heart Valves. J. Comput. Phys., vol. 35, 1980, pp. 183–205.
8. Peskin, S. C.; and McQueen, D. M.: A Three-Dimensional Computational Method for the Blood Flow in the Heart. J. Comput. Phys., vol. 81, 1989, pp. 372–405.
9. Tarbel, J. M.; Gunshinan, J. P.; and Geselowitz, D. B.: Pulse Ultrasonic Doppler Velocity Measurements Inside a Left Ventricular Assist Device. J. Biomech. Engr. Trans. ASME, vol. 108, 1986, pp. 232–238.
10. Mueller, T. J.: Application of Numerical Methods in Physiological Flows. Numerical Methods in Fluid Dynamics. 1978.

11. Idelsohn, S. R.; Costa, L. E.; and Ponso, R.: A Comparative Computational Study of Blood Flow through Prosthetic Heart Valves Using the Finite Element Method. J. Fluid Dynamics, vol. 18, no. 2, 1985, pp. 97–115.
12. Stevenson, D. M.; Yoganathan, A. P.; and Williams, F. P.: Numerical Simulation of Steady Turbulent Flow through Trileaflet Aortic Heart Valves II. Results on Five Models. J. Biomechanics, vol. 16, no. 12, 1985, pp. 909, 926.
13. Rosenfeld, M.; Kwak, D.; and Vonokur, M.: A Fractional Step Solution Method for the Unsteady Incompressible Navier–Stokes Equations in Generalized Coordinate Systems. J. of Comput. Phys., vol. 94, no. 1, 1991, pp. 102–137.
14. Kiris, C.: Computations of Incompressible Viscous Flows through Artificial Heart Devices with Moving Boundaries. Stanford University, Stanford, Calif., 1991.
15. Rogers, S. E.; Kwak, D.; and Kiris, C.: Numerical Solution of the Incompressible Navier–Stokes Equations for Steady-State and Time-Dependent Problems. AIAA Journal, vol. 29, no. 4, 1991, pp. 603–619.
16. Benek, J. A.; Buning, P. G.; and Steger, J. L.: A 3-D Chimera Grid Embedding Technique. AIAA Paper 85–1523, 1985.
17. Pedley, T. J.; and Stephanoff, K. D.: Flow along a Channel with a Time-Dependent Indentation In One Wall: The Generation of Vorticity Waves. J. Fluid Mech., vol. 160, 1985, pp. 337–367.
18. Ralph, M. E.; and Pedley, T. J.: Flow in a Channel with a Moving Indentation. J. Fluid Mech., vol. 190, 1988, pp. 87–112.
19. Baldwin, J. T.; and Tarbell, J. M.: Mean Flow Velocity Patterns within a Ventricular Assist Device. ASAIO Transactions, vol. 35, Sept. 1989, pp. 425–433.

Figure Captions

Figure 1. Instantaneous streamlines: $Re = 600$, $St = 0.057$. (a) $t = 0.45$. (b) $t = 0.55$. (c) $t = 0.65$. (d) $t = 0.75$. (e) $t = 0.80$. (f) $t = 0.90$. (g) $t = 1.5$.

Figure 2. Comparison of numerical results with experimental measurements and other numerical solutions.

(a) Time-evolution of vortices center.

(b) Vortices A, B, C, and D.

Figure 3. Tilting-disk geometry showing valve opening.

Figure 4. Overlapped grids.

Figure 5. Pressure drop across tilting-disk valve versus steady-state flow rate.

Figure 6. Comparison of numerical result and experimental measurements.

Figure 7. Velocity vectors at several longitudinal stations.

Figure 8. Particle traces showing minor and major flow regions.

Figure 9. Vorticity magnitude contours.

(a) Channel surface.

(b) Outflow surface of disk.

(c) Inflow surface of disk.

Figure 10. Side view of velocity vectors on the lateral symmetry plane showing the valve.

(a) $t/T = 0.128$.

(b) $t/T = 0.257$.

(c) $t/T = 0.385$.

Figure 11. Computational grid for Penn State artificial heart model showing zonal and overlapped grid regions.

Figure 12. Unsteady particle traces at $t/T = 0.45$ as pusher plate nears bottom position.

Figure 13. Velocity vectors of incoming fluid at $t/T = 0.375$. Top view in horizontal planes through the center of tubes and in horizontal plane 3 mm below top surface of chamber.

Figure 14. Experimental results at $t/T = = 0.375$ (Ref. 19).

Figure 15. Velocity vectors of incoming fluid at $t/T = 0.625$; top view in horizontal planes through center of tubes and in horizontal plane 3 mm below top surface of the chamber.

Figure 16. Experimental results at $t/T = 0.625$ (Ref. 19).

Figure 17. Velocity vectors of incoming fluid at $t/T = 0.25$; side view in vertical plane through center of inflow tube.

Figure 18. Velocity vectors in the cross-sectional plane of outflow tube showing swirling motion of the fluid: $t/T = 0.75$.

† NASA Ames Research Center, Moffett Field, California 94035.

‡ Stanford University, Stanford, California.

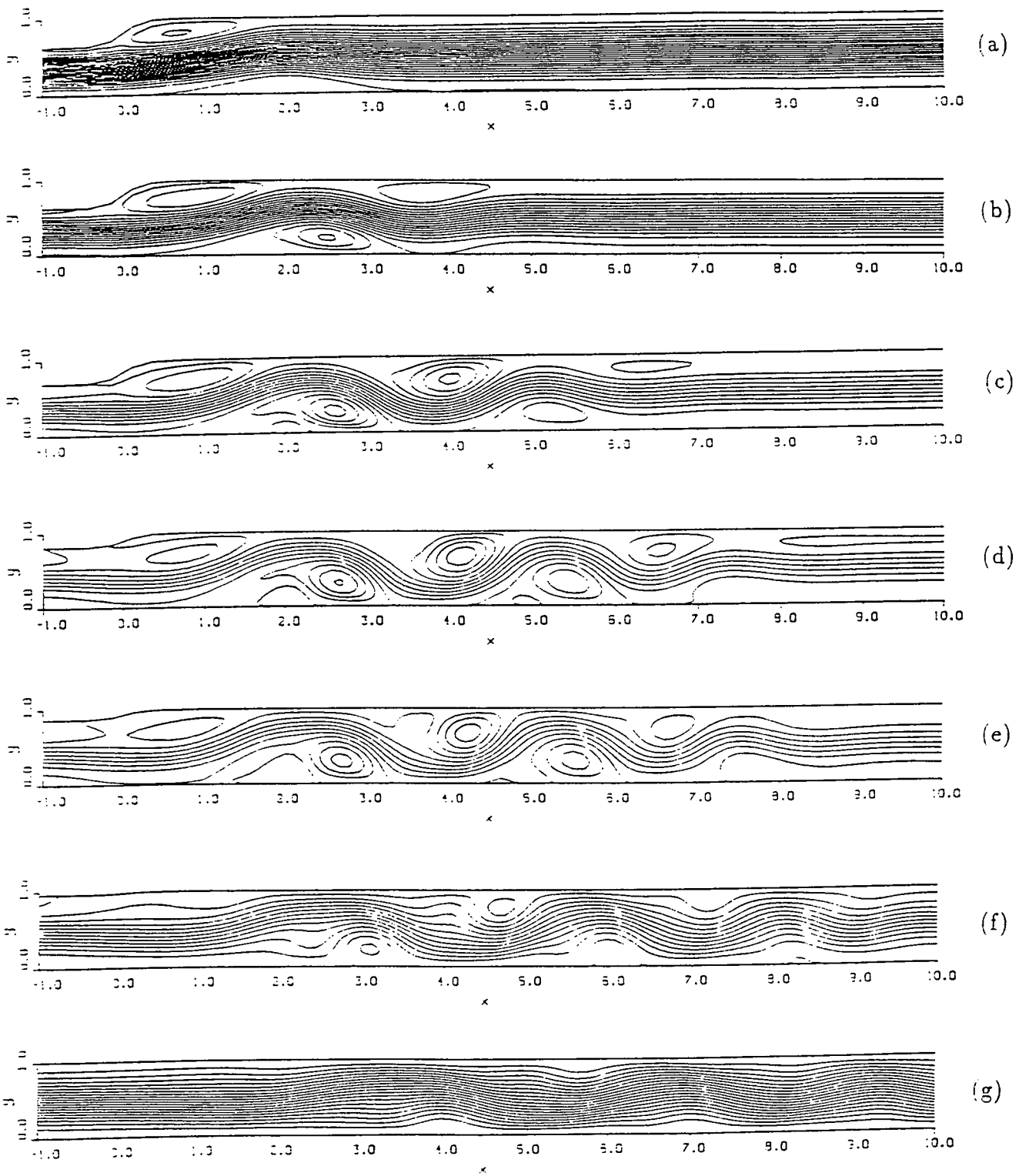

Figure 1: Instantenous streamlines, $Re = 600$, and $St = 0.057$. (a)$t = 0.45$; (b)0.55; (c)0.65; (d) 0.75; (e) 0.80; (f) 0.90; (g) 1.0.

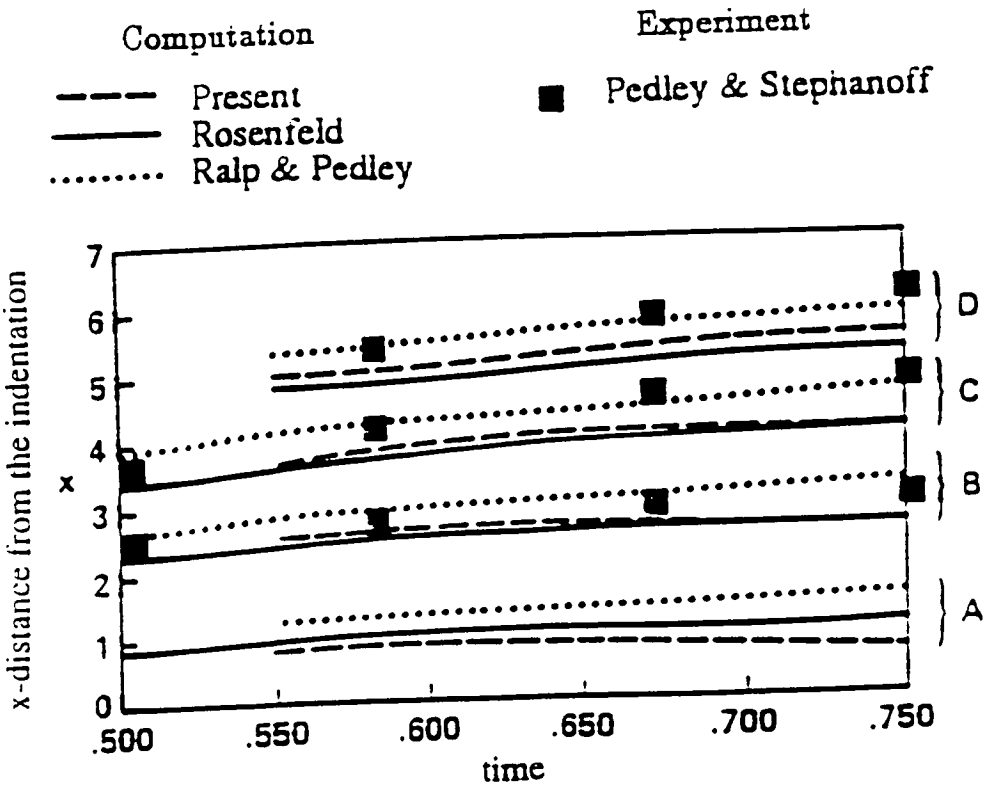

(a) Time evolution of the vortices center.

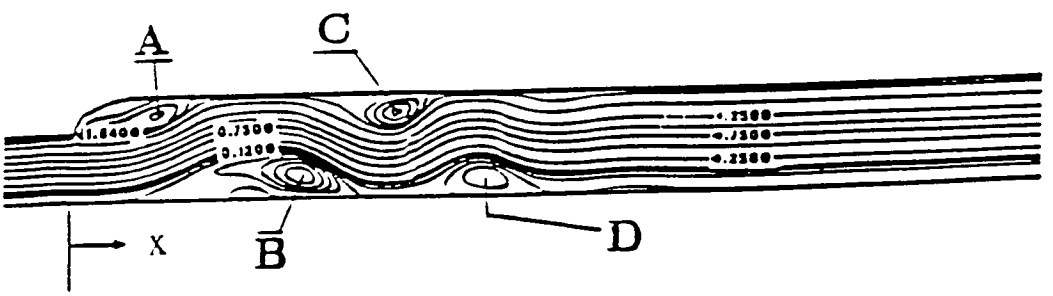

(b) Showing the vorticies A,B,C, and D.

Figure 2: Comparison of the numerical results with the experimental measurements and other numerical solutions.

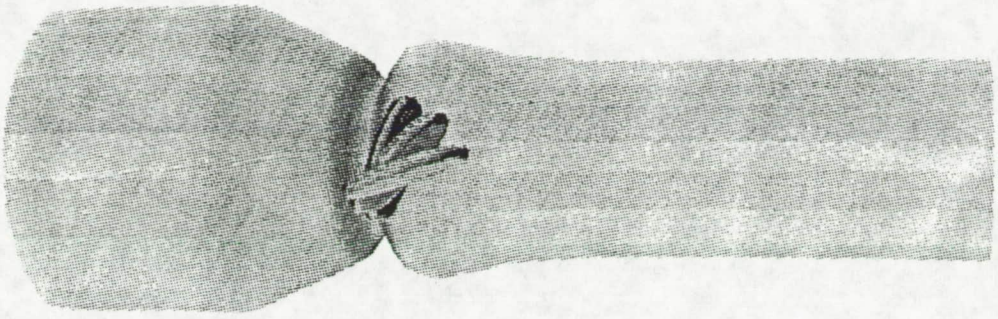

Figure 3: Tilting disk geometry showing valve opening.

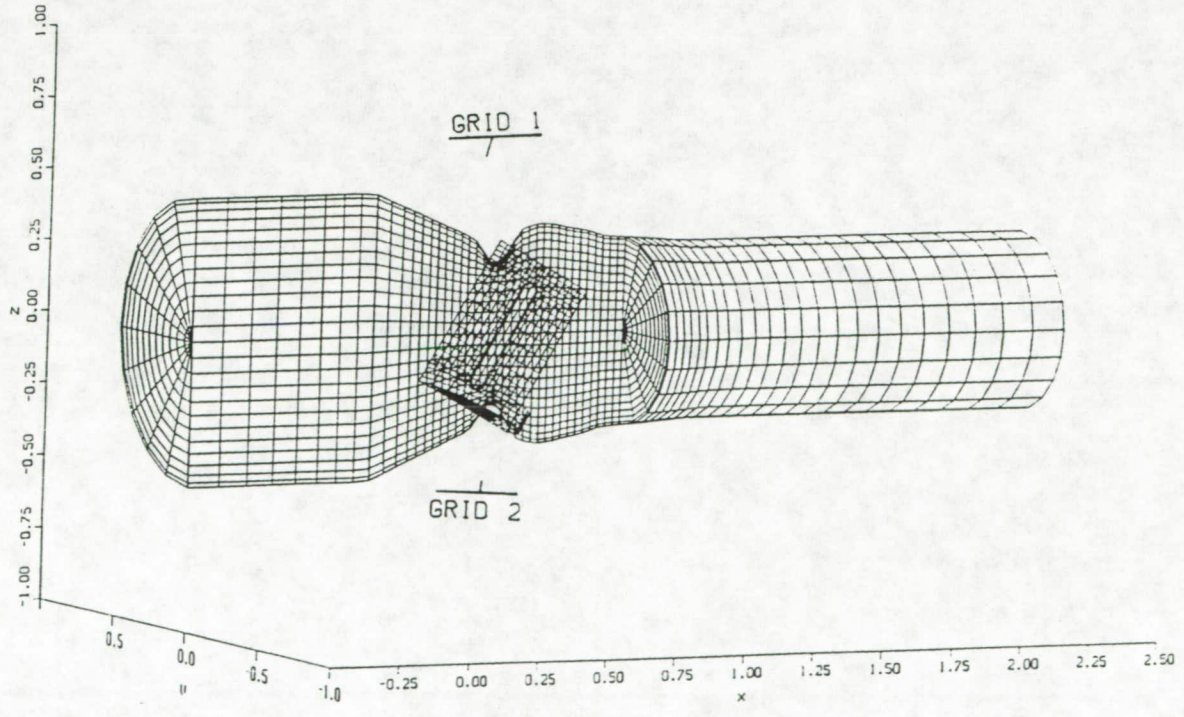

Figure 4: Perspective view of two overlapped grids.

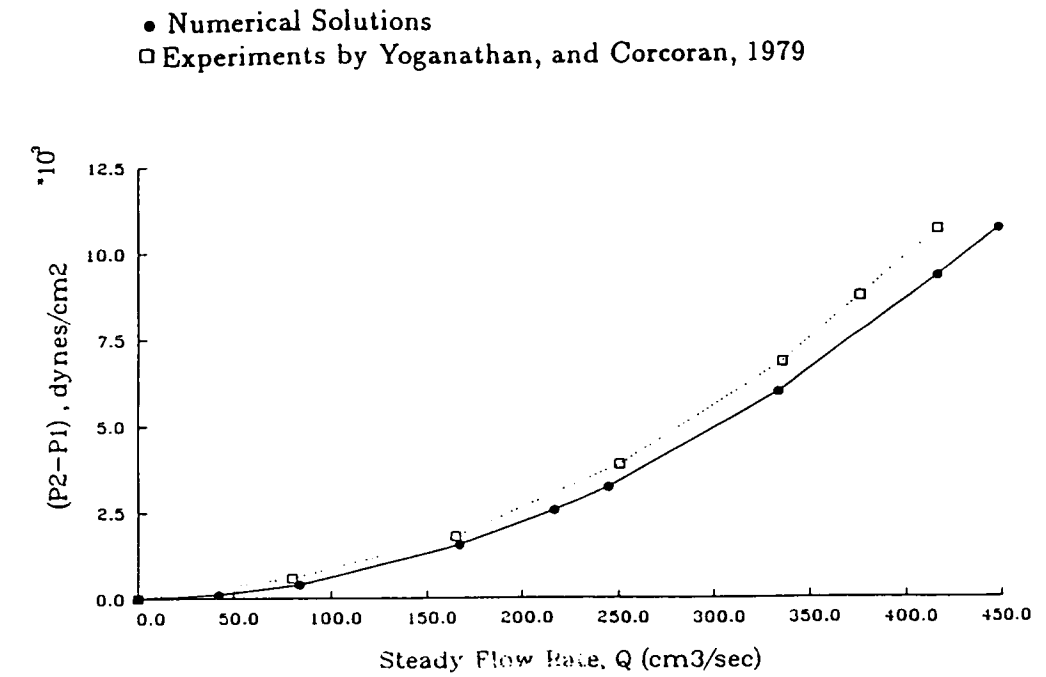

Figure 5: Pressure drop across the tilting disk valve versus steady-state flow rate.

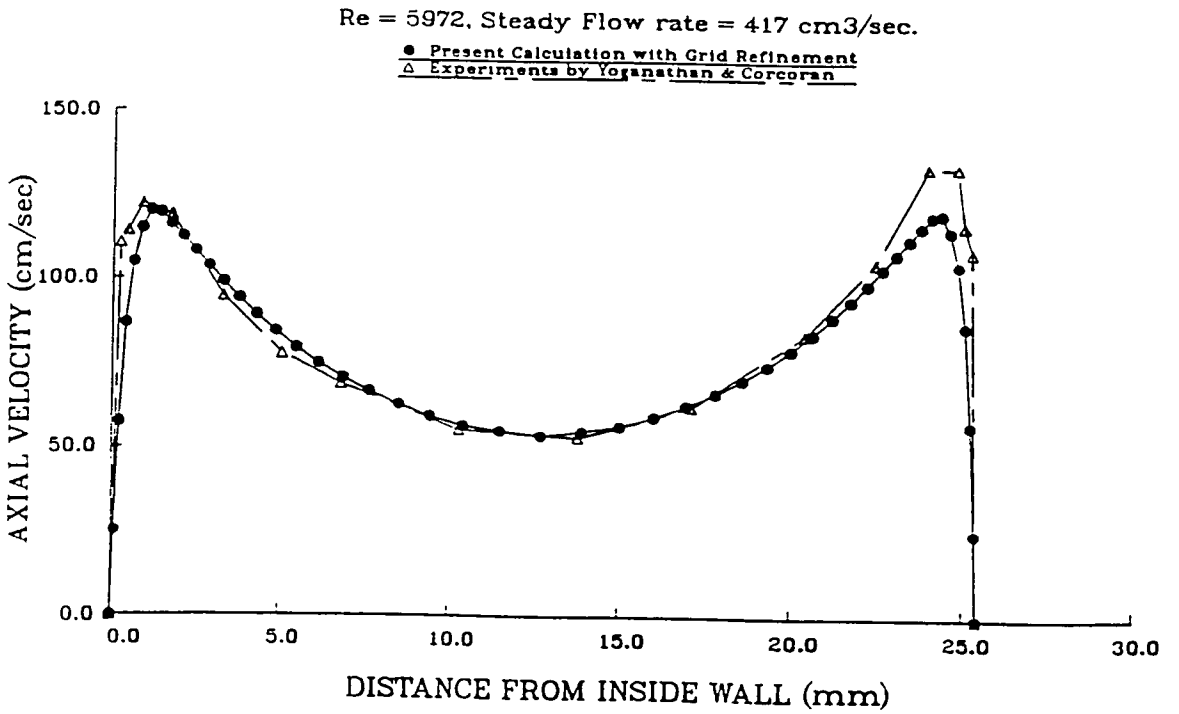

Figure 6: Comparison between the numerical result and the experimental measurements.

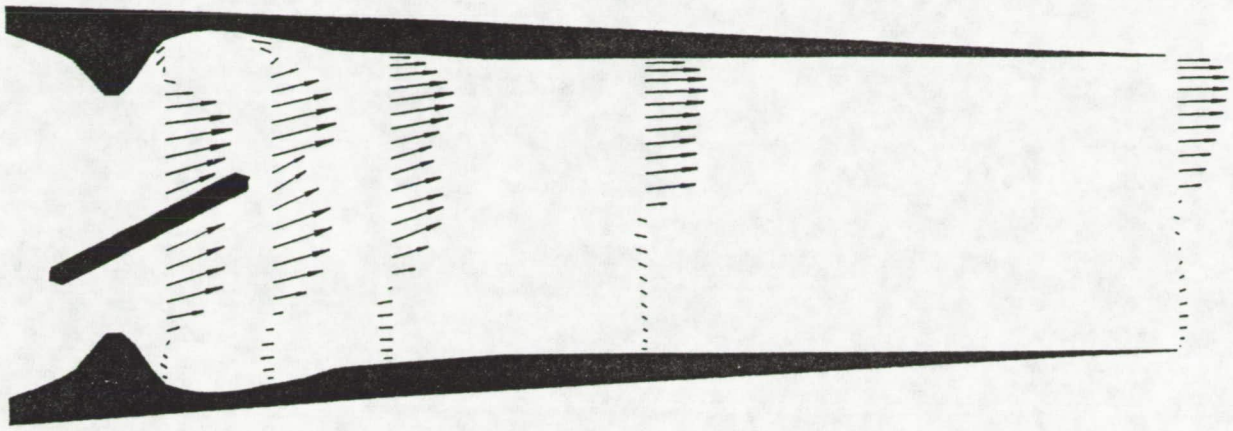

Figure 7: Velocity vectors at several longitudinal stations.

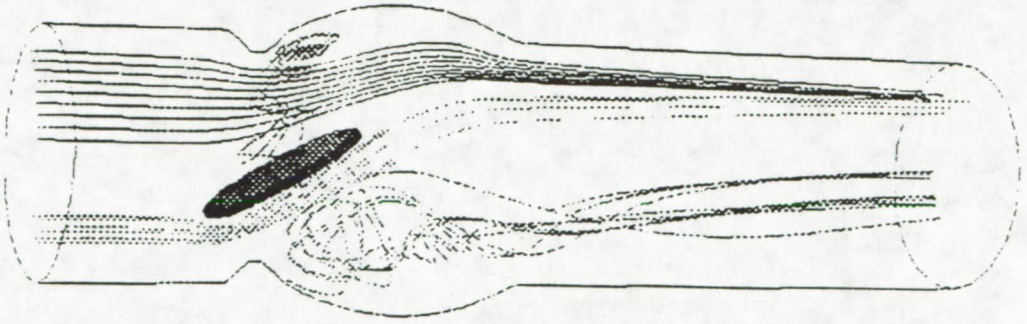

Figure 8: Particle traces showing the minor and the major flow regions.

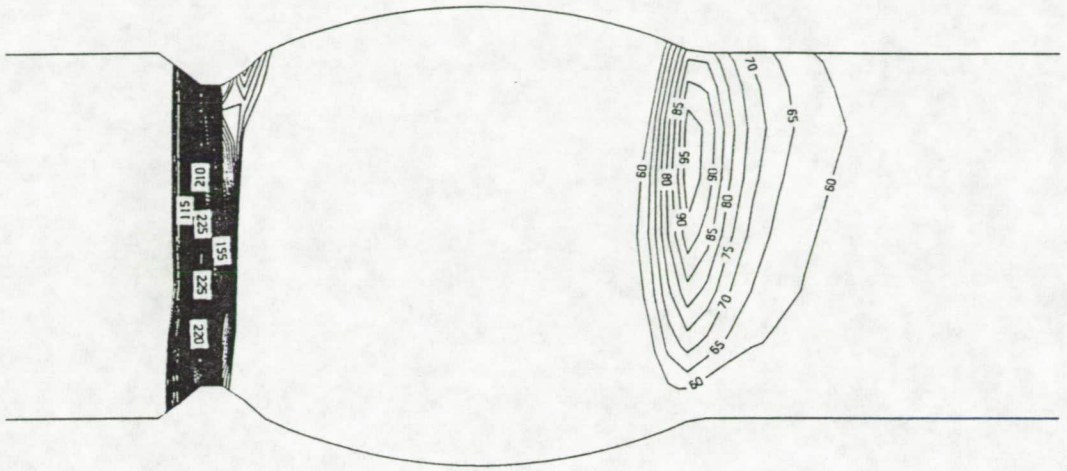

(a)

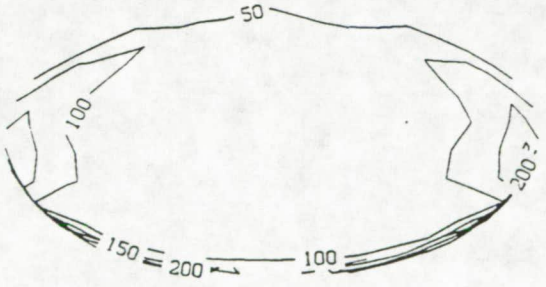

(b)

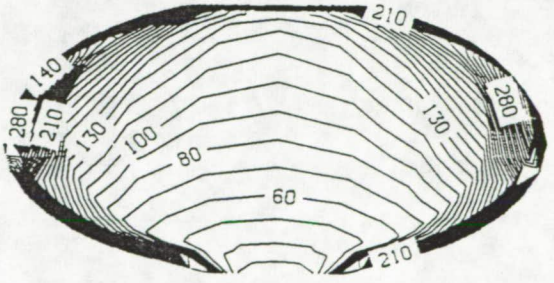

(c)

Figure 9: Vorticity magnitude contours on the (a) channel surface; (b) outflow surface of the disk; (c) inflow surface of the disk.

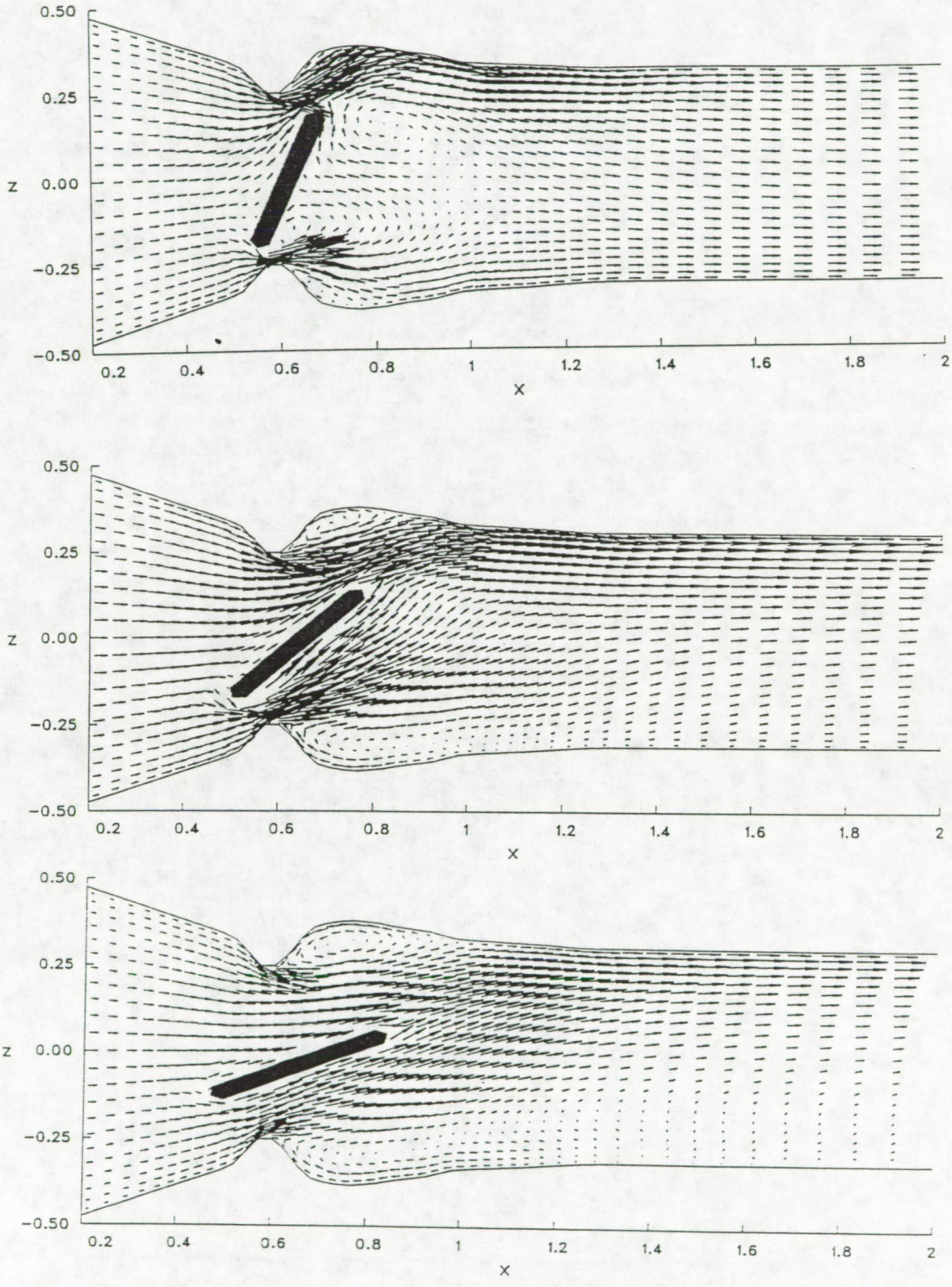

Figure 10: Side view of velocity vectors on the lateral symmetry plane showing the valve openning.

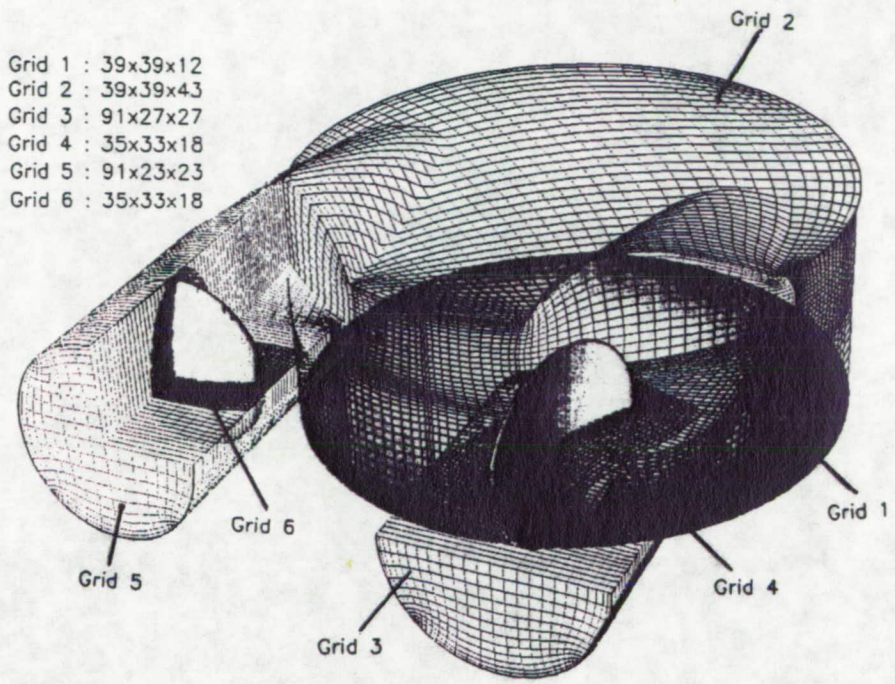

Figure 11: Computational grid for Penn State artificial heart model showing zonal and overlapped grid regions.

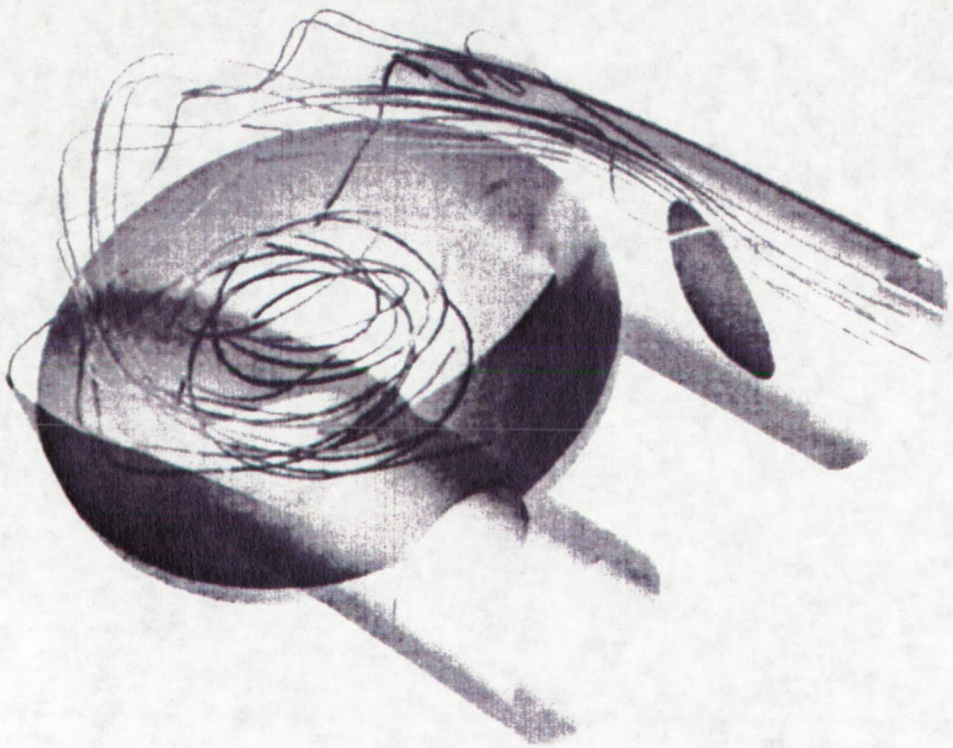

Figure 12: Unsteady particle traces at $t/T = 0.45$ as the pusher plate nears the bottom position.

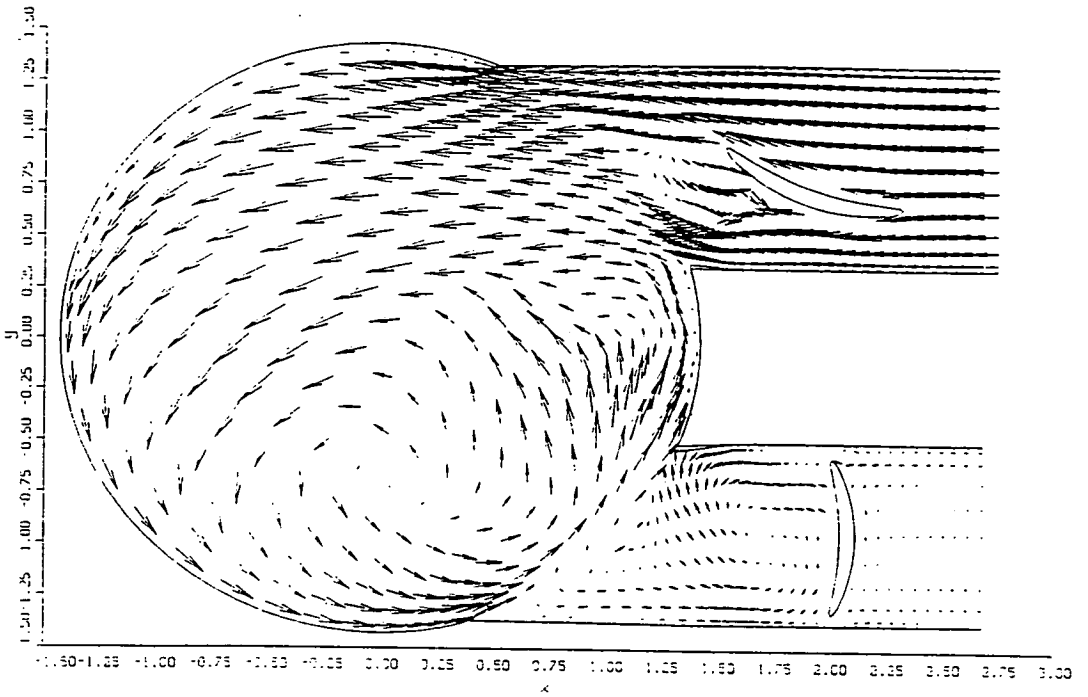

Figure 13: Velocity vectors of incoming fluid at $t/T = 0.375$. Top view in horizontal planes through the center of tubes and in horizontal plane 3 mm. below the top surface of the chamber.

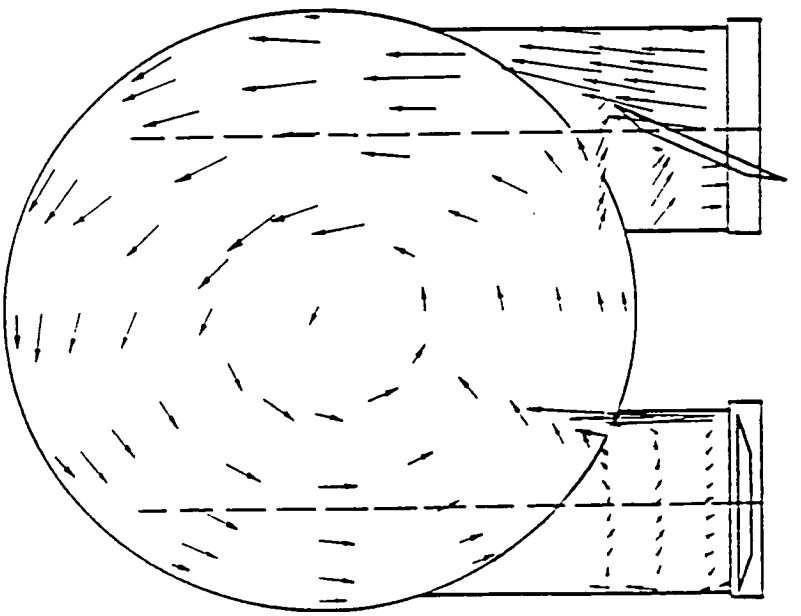

Figure 14: Experimental results at $t/T = 0.375$ by Baldwin and Tarbell (Ref. 19).

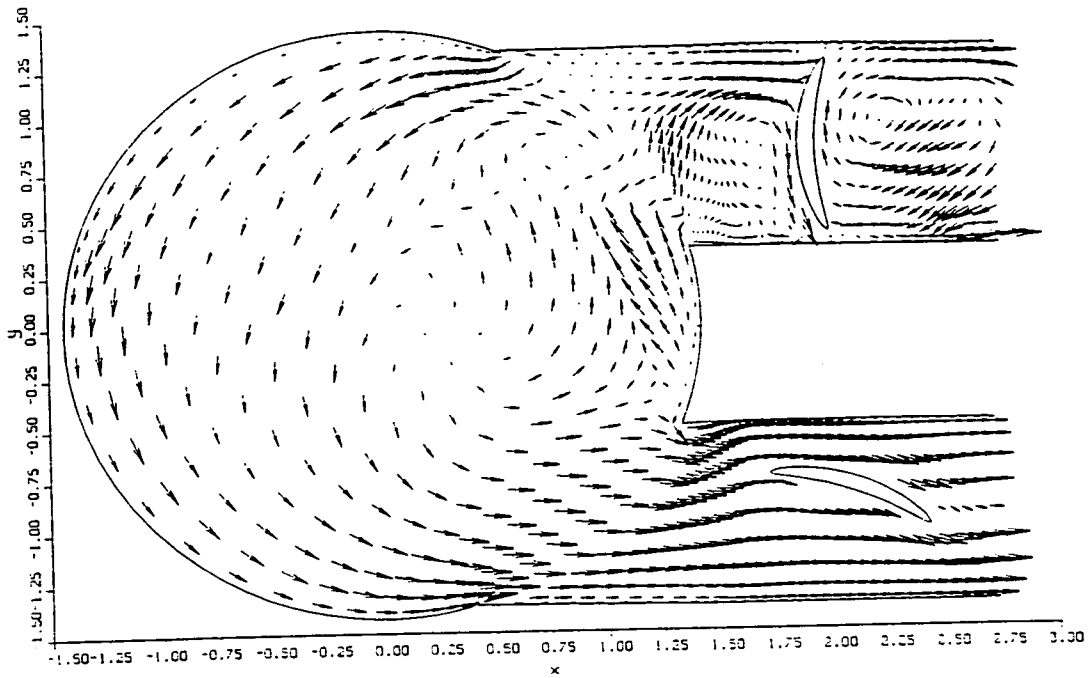

Figure 15: Velocity vectors of incoming fluid at $t/T = 0.625$. Top view in horizontal planes through the center of tubes and in horizontal plane 3 mm. below the top surface of the chamber.

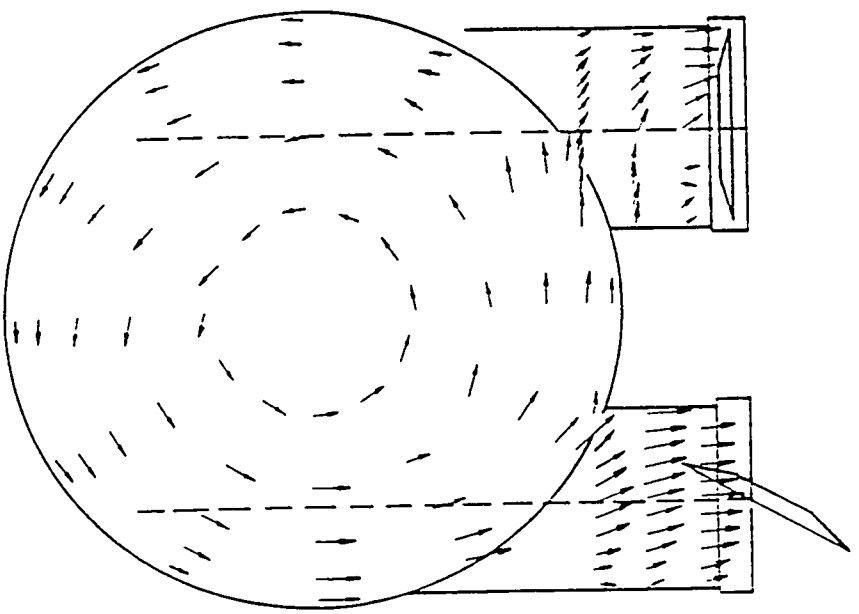

Figure 16: Experimental results at $t/T = 0.625$ by Baldwin and Tarbell (Ref. 19).

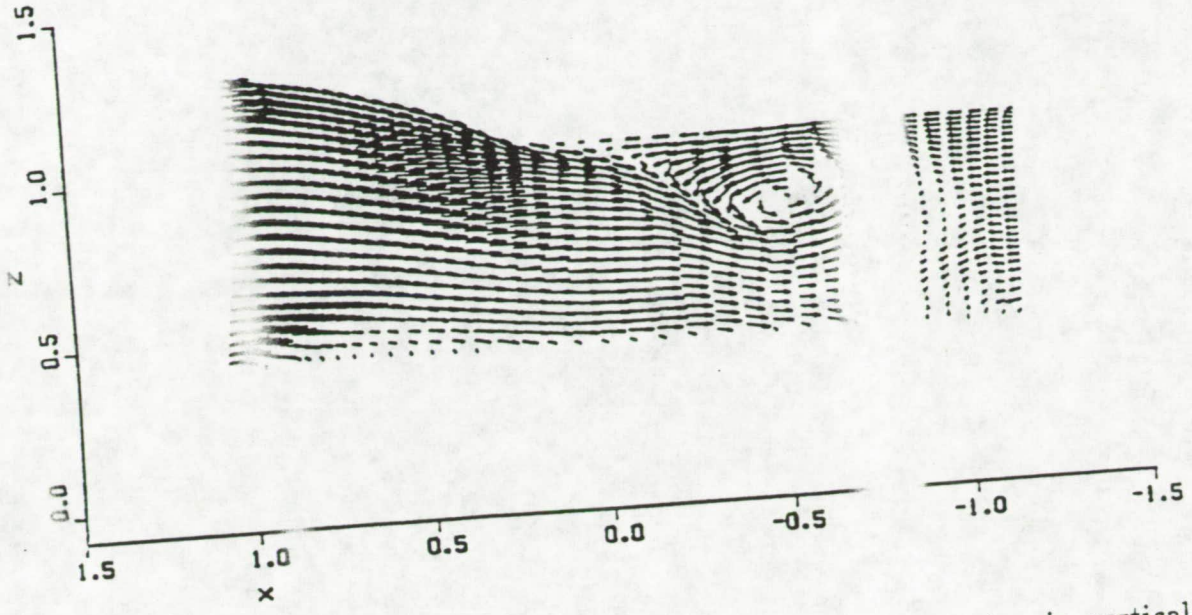

Figure 17: Velocity vectors of incoming fluid at $t/T = 0.25$. le view in vertical plane through center of inflow tube.

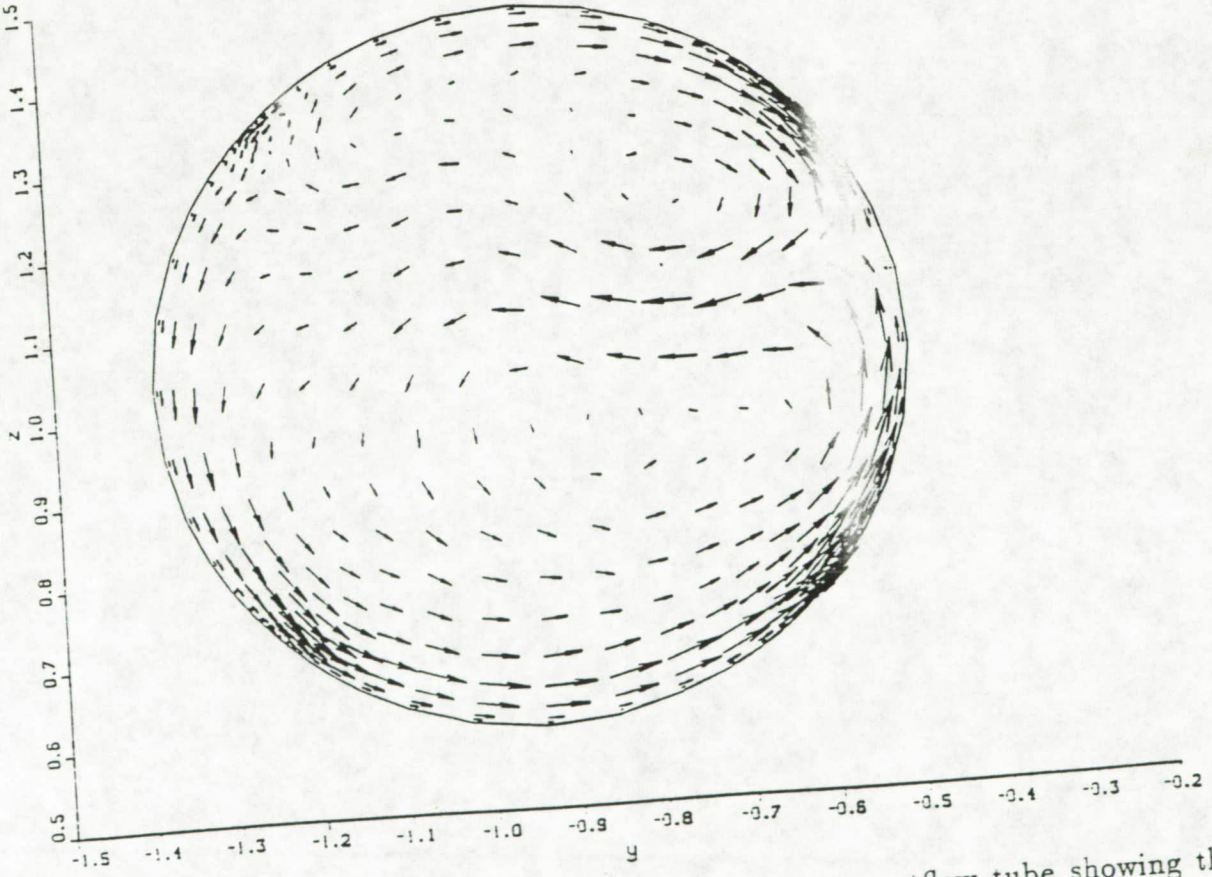

Figure 18: Velocity vectors in the cross-sectional plane of the outflow tube showing the swirling motion of the fluid. $t/T = 0.75$.

MCAT Institute
Final Report 92-003

INCOMPRESSIBLE VISCOUS FLOW COMPUTATIONS FOR THE PUMP COMPONENTS AND THE ARTIFICIAL HEART

Dr. Cetin Kiris

March 1992

NCC2-500

MCAT Institute
3933 Blue Gum Drive
San Jose, CA 95127